Feasibility study of a green energy powered thermoelectric chip based air conditioner for electric vehicles

Á.G. Miranda, T.S. Chen, C.W. Hong*

Department of Power Mechanical Engineering, National Tsing Hua University, Hsinchu 30013, Taiwan

A B S T R A C T

Traditional compressed-refrigerant air conditioning systems consume substantial energy that may reduce the driving performance and cruising mileage of electric vehicles considerably. It is crucial to design a new climate control system, using a direct energy conversion principle, to further aid in the commercialization of modern electric vehicles. A solid state air conditioner model consisting on TECs (thermoelectric chips) as the load, DSSCs (dye sensitized solar cells) as the renewable energy source and high power LiBs (lithium-ion batteries) as an energy storage device are considered for a personal mobility vehicle. The power management between the main power net and the solid state air conditioner interface is designed with an outer proportional-integral controller and an inner passivity based current controller with a loss included model for perfect tracking. This model is intended to comprise thermal and electrical elements which can be tunable for performance benchmarking and optimization of a solid state air conditioning system. Dynamic performance simulations of the solid-state air conditioner are performed, alongside guidelines for feasibility.

© 2013 Elsevier Ltd. All rights reserved.

1. Introduction

TECs (Thermoelectric cooling chips) possess the advantages such as no moving parts, no noise, long life, no refrigerants, small size and precision temperature control [1]. Although they are still lower COP (coefficient of performance) compared to traditional compressed-refrigerant systems, the direct conversion of electric energy into heat transfer is straightforward for engineering considerations. In the work of Rifffat et al. [2], a test system for heating and cooling was constructed with TECs. A discrepancy between the simulation and the experimental results was found to be due to the difficulty of determining an accurate physical model of the TECs, thermal diodes and heat sinks. However, correction factors were devised. Cosnier et al. [3] concluded that a COP higher than 1.5 for cooling and higher than 2 for heating, with a current of 4–5 A and a temperature difference (ΔT) of 5–10 °C, could be obtained using their setup of a TEC system. Maneewan et al. [4] constructed a personal TEC based compact air conditioner and achieved a COP of about 0.34 at a 1 A current and with a cooling capacity of 29.2 W.

The cabin in a personal mobility electric vehicle has limited space, making TECs appropriate over traditional refrigerant air conditioners. TEC based air conditioners must take as an objective

the cooling/heating of individual passengers, not cabins. A special property of this air conditioner is that the same cooling system can be switched to a heating system with a simple polarity reversal of the direct current that supplies the power. Another important use for a thermoelectric chip may be as a waste heat harvester, termed as thermoelectric generators – studied elsewhere [5]. These can be placed at the exhaust pipe of an internal combustion engine to be an auxiliary power supply. However, the engine performance could become a complication depending on the thermal conductivity of the thermoelectric chip [6] because the ability to release heat of the exhaust pipe could be compromised.

A viable power source alternative is the DSSC (dye sensitized solar cell) which doesn't interfere with the performance of an engine or hybrid/electric based vehicle. Although DSSCs are still low in conversion efficiency, maximum is reported at 12.3% [7], compared to traditional silicon-based solar cells which can exhibit an efficiency higher than 42.9% [8], their manufacturing costs are low and the raw materials are abundant. However, they can be improved by means of quantum dot dyes, nanotube TiO_2 electrodes [9], ionic liquids and improved manufacturing methods. Other superiorities of DSSCs are that they are comparatively higher in efficiency than all the other types of solar cells at low light intensities, have a low dependency on the angle of incidence and their efficiency does not decrease as temperature increases [10]; all of which may happen from time to time in vehicle applications. The coupling of thermoelectric modules with a polycrystalline photovoltaic panel for air pre-heating and

* Corresponding author.
E-mail addresses: cwhong@pme.nthu.edu.tw, cwhong@mx.nthu.edu.tw (C.W. Hong).

pre-cooling application was carried out in a one-year-long simulation with the meteorological conditions of Chambery, France, and achieved a COP ranging from 0.096 to 0.23 over one year [11]. They concluded that the direct coupling was not a sustainable option, especially in summer. This is because when the solar irradiance is higher, the current sourced from the solar cells is too high and causes the COP of the TECs to decline. It is of prime importance to design a stable and accurate current control for the DC (direct current)–DC converter; in this case the TECs and/or electric fans. Passivity based controllers were previously used for solar cells to keep the power at a maximum operating point by employing MPPT (maximum power point tracking) methods [12] and passivity based controls [13].

In this paper, DSSCs are considered to be the top auxiliary power source for the TEC air conditioning system to reduce the power supplied by the main power supplies, i.e., the main LiB pack or a fuel cell stack.

2. Research methodology

AC (alternating current) impedance spectroscopy is a test method which is widely adopted to detect the dynamic characteristics for some complicated electrochemical as well as solid state systems. A monochromatic signal $v(t) = v \sin(wt)$ is applied to the system and the resulting current $i(t) = i \sin(wt + q)$ is measured. The use of Fourier transformation allows the simplification of the mathematical treatment of this system. The impedance is designated as a complex variable, which can be plotted on a Nyquist diagram. Experimentally obtained impedance data are analyzed and fitted to an empirical equivalent circuit for several operating conditions. However, this equivalent circuit is still in the frequency domain, $2\pi f$, which is then converted to the Laplace domain, js, and finally transformed to the time domain for a usable impedance circuit. The transformation from the frequency to the time domain is carried out in AUTOLAB's NOVA 1.9 software. Regarding TECs, because of their working principle and the material structure, models should be built up on electrical and thermal parts, and the mutual relationship has to be determined. The solar simulator equipment is composed of a Full Spectrum Solar Simulator, model 91160, which can reach a power output of 2 suns and can simulate various solar conditions such as the common AM (Air Mass)1.5.

On the other hand, the battery pack consists on Lithium ion batteries with LiFePO$_4$ cathode types. The model extraction was done using dynamic discharge tests to fit an accurate equivalent circuit from 1C to 2.5C, where 1C is equivalent to 12 A, following the experimental procedure found in Ref. [14]. However, no analysis on its transient behavior is done in order to focus on the real goal of this work.

3. Mathematical models of the air conditioner system elements

3.1. AC impedance extracted mathematical model of the DSSC

When a DSSC is irradiated by light, the dyes will absorb the energy of light (h) and quantum jumps to the excited state (S^*), the excited electrons will then inject into the conduction band of the TiO$_2$. The dye loses an electron and becomes S^+, which will be oxidized (ox) by the iodine ion in the electrolyte and returns to the initial ground state (S). The tri-iodine is diffused to the cathode and is reduced back to the iodine locally. The overall reaction is summarized below:

$$\text{red} + h\nu \rightarrow \text{ox} + e^- \tag{1}$$

Electrons in the conduction band of the TiO$_2$ will diffuse through the semiconductor and pass to the conductive glass then to the

external circuit and arrive at the cathode. At the cathode, the electron will transfer to the tri-iodine ion and reduce (red) it back to the iodine. Through the diffusion transportation in the electrolyte due to a concentration gradient, the iodine will move towards the anode and is oxidized to tri-iodine again. The entire reaction is cyclic and the diffusion rate is the rate-limited process of the overall reaction.

The major problem with a voltage dependent current source DSSC, is that it is counter-intuitive for power systems. The output voltage of the DSSC must be known to calculate the output current. However, in power systems, the output load is already known and the output voltage of the DSSC must be calculated. If the demanded current load reaches the I_{sc} then the voltage will become zero and no more power will be output by the DSSC. Instead of solving for the typical solar cell diode equation, which is a current source, a different perspective is applied; the DSSC can be seen as one current source and two current sinks. By solving this current loop, the output current (I_{DSSC}) can be drawn from the DSSC and inverted to a voltage source, V_{DSSC}, as follows:

$$\begin{aligned}
f &= [I_b + I_d]/1000 \\
I_{sc}I_{sc\_rel}f &- I_{DSSC} - V_{DSSC}/(R_{th}V_{oc\_rel}) = 0 \\
\therefore V_{DSSC} &= (I_{sc}I_{sc\_rel}f - I_{DSSC})R_{th}V_{oc\_rel}
\end{aligned} \tag{2}$$

where f captures the fundamental effect of the total absorbed irradiance of the DSSC by employing the beam and diffuse irradiance, I_b and I_d, respectively, and normalized to the tested AM1.5 irradiance of 1000 W m^{-2}. An issue to note is that for silicon solar cells, I_b must be multiplied by the cosine of the angle of incidence, whereas for the DSSC case, V_{oc_rel} and I_{sc_rel} are parameters which are to be obtained in order to capture the effects of the angle of incidence; these are further studied in the Results and Discussion section. The R_{th} term is the Thevenin resistance term that is composed of the serial combination of the three effective resistances to be discussed later and is dependent on V_{DSSC}, and operating temperature, T_{DSSC}. A point to highlight about silicon and crystalline solar cells [15] is the negative effect that high temperatures may cause. This can be alleviated if a TEC and silicon solar cell module have water flowing between the heat regeneration channels that separate both devices [16]. This arrangement would, however, increase the balance of plant and defeat the purpose by taking care of a power source.

3.2. The TEC and cabin system model

The main theories of thermoelectricity are based on the Seebeck effect and the Peltier effect; both phenomena are a direct conversion between thermal and electric energy [17]. A temperature gradient can be generated by applying a direct current, operating as a heat pump; in the same manner a direct current can be generated through a temperature gradient and operate as an electric generator. The structure of the TEC is illustrated inside the dashed rectangle in Fig. 1. There are pairs of junctions which are connected electrically in series by metallic interconnectors and thermally in parallel between two heat sinks. As thermoelectric materials, the n-type and p-type semiconductors are used, which may include Sb–Te, Bi–Te, or Si–Ge compounds. The operation principle of the TEC, as a heat pump, begins when a direct current is supplied from the p-leg through a metal interconnector to the n-leg, the electron and electron-hole flows are all from the absorbing side to the emitting side. Heat will be absorbed at the T_a side and be emitted at the T_e side; T_a is the side where positive voltage is applied to. Using this principle, an air conditioner can be designed without any moving parts, except for the fans in the vehicle cabin. By controlling the
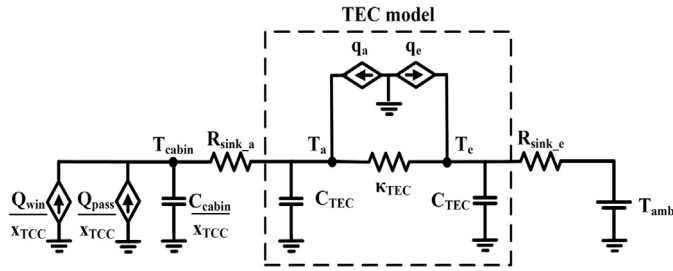
Fig. 1. Equivalent circuit diagram of the TEC air conditioner system and cabin model for the cooling case. The a and e subscripts are interchangeable depending on the operation mode.

input DC current, I_{TEC}, it is possible to control the amount of heat absorption or emission.

The rest of the schematic of the thermoelectric air conditioner design for an electric vehicle is shown in Fig. 1 (outside the dashed rectangle), which is a thermal analogy of the cabin and TEC module system. The denominator, x_{TCC}, translates into the number of TECs that cooperate to reduce the strain on the TEC system and increase the COP_x, where the subscript x may represent absorbing heat or emitting heat modes, which can be represented as follows:

$$COP_{a,e} = \left| \left[q_{a,e} - (T_{a,e} - T_{e,a}) \kappa_{TEC}^{-1} \right] V_{TEC}^{-1} I_{TEC}^{-1} \right| \tag{3}$$

where thermal conductivity effect is represented as κ_{TEC}. The coupling heat transfer relationship is embedded in the sum of two terms, q_e and q_a, at the emitting (hot) and absorbing (cold) sides of one TEC are:

$$q_e = q_e^Q + q_e^\Pi = \tfrac{1}{2} I_{TEC}^2 R_{TEC} + S T_e I_{TEC}$$
$$q_a = -q_a^Q + q_a^\Pi = -\tfrac{1}{2} I_{TEC}^2 R_{TEC} + S T_a I_{TEC} \tag{4}$$

where the Q and Π superscripts refer to the ohmic resistance, R_{TEC}, losses during current conduction and the Peltier effect depending on the S term (Seebeck coefficient) corresponding to the p-leg and n-leg material properties, respectively. In order to obtain the aforementioned parameters, the readers are referred to equations (23–24) in Ref. [18]. It is very important to notice that when working in the emitting heat mode, the COP is clearly higher than in the heat absorbing mode which points out the advantage of the heating mode over the cooling mode for TECs. The thermoelectric elements and ceramic plates of each TEC also contain a heat storage capacitor, C_{TEC}, which is the capacity to store heat in the ceramic plates and the thermoelectric element pellets; this value is taken as 5.68 J K^{-1}, as in Ref. [18]. Moreover, T_{cabin} and T_{amb} represent the cabin and the outside temperature, respectively. The interface between the TEC modules and the cabin/outside environments is given by the equivalent sink resistances, R_{sink_x} (subscript x refers to the absorbing or emitting sides), which need to be as small as possible. In reality a DC or AC fan is implemented for forced convection. In this study, the applied fan power vs. air velocity ($v_{fan,in}$ m s^{-1}) relationship and the produced air velocity vs. heat dissipation resistance of the sink (R_{sink}) are taken as:

$$v_{fan} = -1.265 P_{fan}^{-0.6131} + 3.138$$
$$R_{sink} = 0.9552 \exp\left(-1.631 v_{fan}\right) + 0.1616 \tag{5}$$

where P_{fan} is the input power of the fan.

The first equation may be taken from the 6010 fan model datasheet manufactured by QWIKFLOW®, 12 V operating voltage;

the pulse width modulation duty cycle must be tuned to output the desired power. This power/velocity relationship was validated by using a TF-4000 thermal mass flow meter (Tokyo Keiso Co.) and a standard multi-meter. It was seen that the data fitting is correct. The second equation is taken from the 74590 sink model (14 fins) from AAVID THERMALLOY®, whose dimension is $50.8 \times 50.8 \times 50.8$ mm^3 and is connected in series with five more sinks of the same kind to produce a 304.8 mm length sink. The minimum sink thermal resistance of this series sink is around 0.173 W K^{-1} when the fan power is drawing 2.64 W at 12 V from the power net bus. It is noted that two fans are needed per six TECs and therefore, 5.28 W must be drawn per every six TECs.

The cabin is modeled as a lumped capacity parameter, C_{cabin}. The other environmental heat sources are the heat coming from the windows, Q_{win}, and the heat emanated from the passengers, Q_{pass}, which is 60 W according to the data proposed by ASHRAE Standard 55 and multiplied by the number of passengers. These relationships are given in the following equations:

$$C_{cabin} = (V_{cabin} - V_{pass}) \rho_{air}^{-1} C_{p\_air}$$
$$Q_i = (I_b \cos \theta) A_i$$
$$Q_{win} = \sum_{i=1}^{num} (T_{cabin} - T_{env}) A_i \left(h_{in}^{-1} + l \kappa_{win}^{-1} + h_{env}^{-1} \right)^{-1} + (1 - M) Q_i \tag{6}$$

where V_{cabin}, V_{pass}, ρ_{air} and C_{p_air} refer to the cabin volume, volume of all the passengers, air density and air heat capacity. In addition, A_i, h_{in}, l, κ_{win}, h_{env}, M and Q_i are the area of the ith window in m^2, window inner side heat transfer coefficient (25 W m^{-2} K^{-1}), window thickness (5E-3 m), window thermal conductivity (0.5 W m^{-1} K^{-1}), window outer heat transfer coefficient (25 W m^{-2} K^{-1}), window polarization or masking coefficient (0–1 value and equal to 0.87 in this case) and heat incident on the window dependent on the angle of incidence, θ. κ_{win} and M are crucial for the air conditioner performance; the former should be as small as possible and the latter should be as large as possible to effectively diminish the effects of the environment on the cabin interior.

In addition, it has been seen experimentally that the cabin temperature is influenced by the different types of car solar reflective shell colors [19]. In that paper, the silver solar reflective shell with a solar reflectance, ρ, equal to 0.6 can help lower the effects of the solar irradiation on the cabin temperature when compared to others. However, because the DSSC module is placed on top, it is assumed that it blocks the heat incident from the sun. In addition, the heat from the doors can also be added, but neglected in this study because they are also designed to counteract the effects of the environment.

3.3. Loss included passivity based current control of the TEC interface

The car industry has been shifting to an onboard power net of 48 V to reduce the power losses and weight of the internal wiring. This auxiliary power net may be used for brake-by-wire, electric power steering systems, in addition to the heating, ventilation and air condition system. A TEC module will be destroyed if such a voltage is applied to its terminal and therefore, a buck converter must interface the power bus voltage and the TEC module. In this study, the air conditioning module is composed of several TECs in series and thus, sharing the same terminal voltage, as seen in Fig. 2. An EL (Euler-Lagrange) framework [20] is a practical model extractor for switched power systems and therefore, will be applied to develop the buck converter current controller. However, modeling errors may translate into steady state errors, especially at
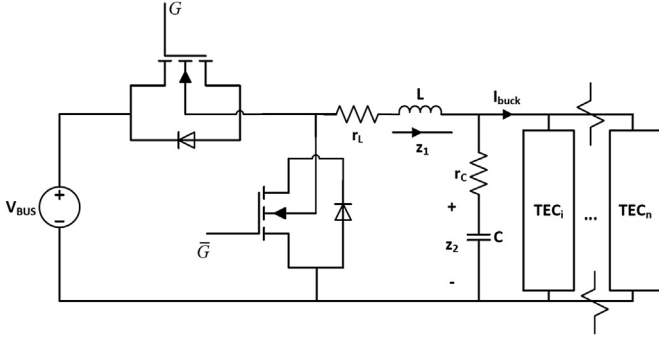
Fig. 2. Buck converter interface between the power net bus and the TECs. Losses for each element of the buck converter are accounted for.

higher currents, and therefore, losses will be taken into account. The averaged EL equations are given as follows:

$$T_{\overline{\mu}}(\dot{q}_L) = \tfrac{1}{2}L\dot{q}_L^2 \quad V_{\overline{\mu}}(q_C) = \tfrac{1}{2C}q_C^2 \quad F_{\overline{\mu}} = [\,\overline{\mu}V_{BUS} \quad 0\,]$$

$$D_{\overline{\mu}}(\dot{q}_L, \dot{q}_C) = \tfrac{1}{2}(r_{MOS}+r_L)\dot{q}_L^2 + \tfrac{1}{2}r_C\dot{q}_C^2 + \tfrac{1}{2}R_{TEC}(-\dot{q}_L + \dot{q}_C)^2$$

$$r_{MOS} = \overline{\mu}r_{MOS1} + (1-\overline{\mu})r_{MOS2}$$

(7)

where the $\overline{\mu}$ subscript is taken as an averaged value of the switched state of the power MOSFETs, T and V are the kinetic and potential energies of the dynamic circuit, F contains forcing functions associated to the $[q_L\ q_C]$ coordinates, and D is the Rayleigh dissipation function. In addition, r_{MOS1} and r_{MOS2}, r_L, r_C and R_{TEC} are the "on" resistance of the power MOSFETS 1 and 2, inductor series resistance, capacitor series resistance and the effective TEC resistance, respectively. The last term is simply the ratio of the *measured* applied voltage and current on the TEC module(s). The average system description may be obtained after applying the constraint form of the EL equations "by choosing the currents corresponding to the inductive elements and either the charge or the voltage corresponding with the capacitive elements" [20], and is given as follows:

$$\dot{z}_1 = -\frac{(r_{MOS}+r_L+R_{TEC})}{L}z_1 + \frac{R_{TEC}(R_{TEC}z_1 - z_2)}{L(r_C+R_{TEC})} + \frac{\overline{\mu}V_{BUS}}{L}$$

$$\dot{z}_2 = \frac{R_{TEC}}{C(R_{TEC}+r_C)}z_1 - \frac{1}{C(R_{TEC}+r_C)}z_2$$

(8)

where z_1 and z_2 are the inductor current and the capacitor voltage. Note that if the circuit losses are ignored, equation (8) reduces to the one given in Ref. [21].The dynamic controller will regulate the TEC according to the demanded current which must not exceed the maximum limits of the TECs; the same care must be taken for the TEC voltage. The average duty cycle which will track the reference inductor current signal is obtained by applying energy shaping and damping injection procedures [21] where one of the controlled states is directly made to converge its demanded signal. The average duty cycle is in the form of:

$$\overline{\mu} = \int \left(\begin{array}{c} \frac{-\overline{\mu}(r_C+1)}{C(r_C+R_{TEC})} - \frac{-\overline{\mu}R_i}{L} \\[6pt] -\frac{I_{dem}r_C(R_i+r_L+r_{MOS})-R_ir_Cz_1}{R_{TEC}V_{BUS}C(r_C+R_{TEC})} \\[6pt] +\frac{I_{dem}(R_i+r_L+r_C+r_{MOS}+R_{TEC})-R_iz_1}{V_{BUS}C(r_C+R_{TEC})} \\[6pt] +\frac{r_CR_iz_1(r_L+r_{MOS}+R_{TEC})+R_iR_{TEC}(r_Lz_1+r_{MOS}z_1+z_2)}{V_{BUS}L(r_C+R_{TEC})} \end{array} \right) dT_s$$

(9)

where $\overline{\mu}$ will be calculated at every sampling time, T_s; I_{dem} is the demanded reference current and R_i is the damping injection

coefficient strictly positive), which will force an asymptotic stability of the system. The readers are encouraged to compare this formula with that of [21], if interested. This loss-included average duty cycle may seem complicated, but it is mainly composed of constant parameters which are readily available from datasheets provided by the manufacturer; alternatively, AC impedance spectroscopy methods may be employed. An additional observation is that, strictly speaking, z_1, cannot be directly measured and it is assumed that this state is equivalent to the measured output current. The same situation is applied to z_2, which is also assumed to be equal to the measured output voltage of the buck converter. However, it will be seen that these assumption are valid, even if the realistic losses presented later are taken.

4. Results and discussion

4.1. AC impedance results of the DSSCs

The DSSC studied here is a mini high efficiency laboratory DSSC with an active area of 0.283 cm^2 and manufactured by Solaronix. In order to study the behavior of this DSSC, an initial AC impedance test was conducted on under no light conditions, $I_b = 0$
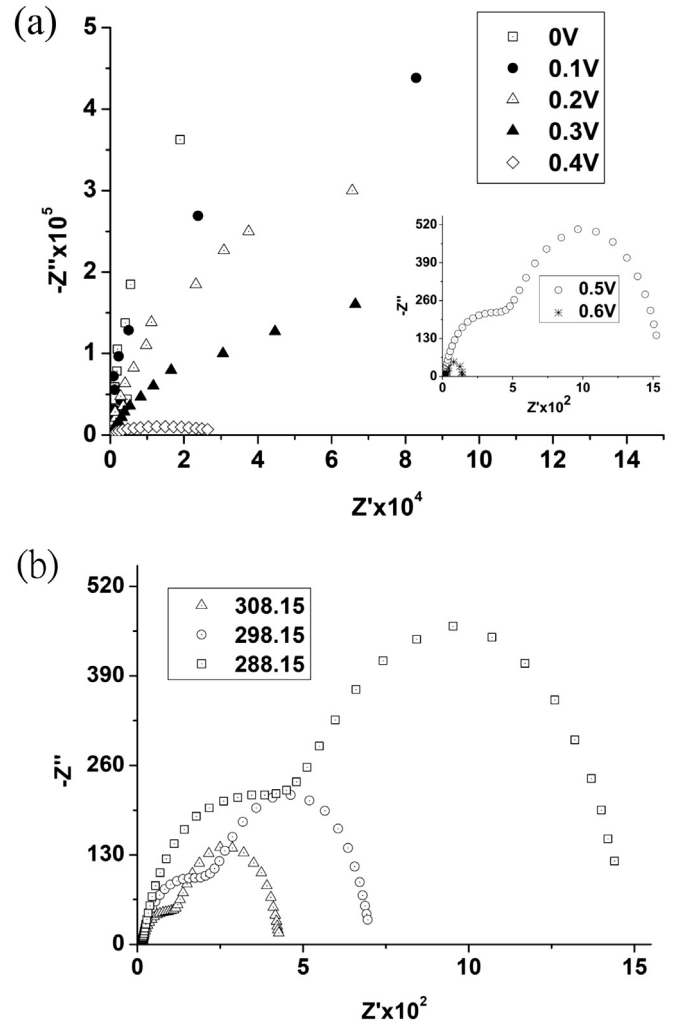

Fig. 3. The Nyquist diagram of the AC impedance test result of the DSSC at (a) 288.15 K and different bias voltages (from 0 to 0.6 V at the interval of 0.1 V); inset shows the 0.5 and 0.6 V bias response. (b) 0.5 V bias voltage and different operating temperatures in K.

W m^{-2}, 0 to 0.6 V bias voltages at the interval of 0.1 V and a measured operating temperature of 288.15 ± 1 K; results are shown in Fig. 3(a). The frequency range in the dynamic test scanning range begins at 100 kHz and ends at 0.1 Hz; the sample number is set as 50. The abscissa is the real part, Z', while the axial is the negative imaginary part, Z''. It was seen that when the frequency is above 100 kHz, the major resistance. always present in the other frequencies, lies at the transparent conductive oxide and its interface with the TiO$_2$ film, which is termed as R_h. When the frequency is in the range from 105 to 10 Hz, the major resistance comes from two parts: one is the reduction reaction between the catalyst Pt on the counter electrode and the electrolytic solution (termed as Z_1); the second part is from the interface of electrons and dyes, the TiO$_2$ electrode, and the electrolytic solution (the combination is termed as Z_2). When the frequency is below 10 Hz, its impedance is thought to be the diffusion resistance in the electrolytic solution, which indicates that the mass transfer impedance (Z_3) is more prominent. The inset in Fig. 3(a) shows that the impedance at the bias voltage 0.5 V is clearly a combination of two semi-circles, which are Z_1 and Z_2. Under such operating conditions, the Nyquist plot indicates that the mass transfer impedance and the interface impedance of the TiO$_2$ and the electrolytic solution couples at the medium and low frequencies. In this case, the mass transfer is relatively small and can be neglected. However, when the bias voltage is smaller than 0.4 V, the influence of Z_2 on the diagram has completely covered the high frequency part. As the bias voltage is set smaller, especially at frequencies lower than 10 Hz, an unstable drift will start to become significant due to the mass transfer effect; this is a threshold voltage and will limit the subsequent experiments from 0.6 to 0.4 V.

After knowing the bias voltage range to be applied, the effects of different temperatures are to be additionally studied. In order to do this, the DSSCs were placed in an incubator under 288.15, 298.15 and 308.15 K conditions in no light conditions and in bias voltages from 0.6 to 0.4 V in a 0.1 V interval; results for the 0.5 V bias case are shown in Fig. 3(b). As expected, higher temperatures will result in lower resistances, which increase the efficiency of the DSSC. The complete results are shown in Table 1. The no light conditions must be normalized to the 298.15 K to be further matched to the AM1.5 results with the specific bias voltage. The mass transfer impedance, Z_3, is generally too small and was confirmed in these experiments and thus, neglected. Only the real part of these relationships are taken into account because the influence of the imaginary part is too small and therefore Z_1 and Z_2 will be referred to their real parts, i.e., R_1 and R_2, respectively. The AM1.5 short circuit current, I_{sc}, is averaged to be 4.81 mA at 298.15 K and R_h is averaged to be 50.8 Ω,

Table 1
AC impedance test results for the DSSC resistances under different operating conditions under dark current and solar cell mode. The AM1.5 condition was performed under a 298.15 K temperature.

Bias [V]	T_{DSSC} [K]	R_2	R_3
0.6	288.15	22.58	107.6
	298.15	14.04	69.71
	308.15	9.32	48.1
	AM1.5	28.88	99.87
0.5	288.15	564.1	912.1
	298.15	250.07	477.2
	308.15	119.85	323.75
	AM1.5	60.32	387.15
0.4	288.15	11,190	22,150
	298.15	3896	8781
	308.15	1455.5	4533
	AM1.5	324.22	2329.57

Table 2
Equivalent DSSC coefficients for equation (10).

R_1 (a, b, c, d, e, f)	34,896, −12.09, 329.36, −1.375, −0.0029, −0.0018
R_2 (a, b, c, d, e, f)	1,177,812, −15.75, 0.0307, 1.6997, 0.0023, −0.1113

whereas the fitting of the other two resistors is shown in the following equations:

$$R_{1,2} = a \exp(bV_{DSSC})[A \exp(nT_{DSSC})]$$
$$A = cT_{DSSC}^d \qquad\qquad (10)$$
$$n = eT_{DSSC}^f$$

where the fitted values are given in Table 2. In addition, the clear advantage of DSSCs over silicon solar cells lies in the low dependency of both the I_{sc} and V_{oc}. The angle of incidence of the solar simulator was varied and the effects on the V_{oc_rel} is given in the following polynomial equation:

$$V_{oc\_rel} = -0.061\,\theta^3 + 0.052\,\theta^2 - 0.026\,\theta + 1 \qquad (11)$$

where θ is the angle of incidence and given in radians, where 0 radians results when the rays of the sun are perpendicular to the DSSC module surface. I_{sc_rel} shows a typical power relationship and therefore, a temporary term, φ (units in rad^{-1}) was created with the following polynomial:

$$I_{sc\_rel}/(\theta_2) = \varphi = -0.08377\,\theta_2^3 + 0.9286\,\theta_2^2 - 3.4725\,\theta_2 + 4.6612$$
$$\theta_2 = \theta + \pi \qquad\qquad (12)$$

where θ_2 exists in order to avoid divisions by zero. These results are shown in Fig. 4. The readers are pointed to see a great resemblance with a typical fuel cell polarization curve if φ is plotted versus θ_2 in a logarithmic plot. For further information on technical measurements of DSSCs and their comparisons with silicon solar cells, please refer to [22]. To validate these results, experimental I–V curves of the DSSC under no light conditions diode mode and different operation temperatures are compared to the simulated counterparts in Fig. 5 (left). It can be noted that it has a very acceptable match between both. Finally, after applying equation (10), the DSSC model can be simulated and compared to the experimental measurements which are shown in Fig. 5 (right). It is noted that a discrepancy between the simulation and experimental
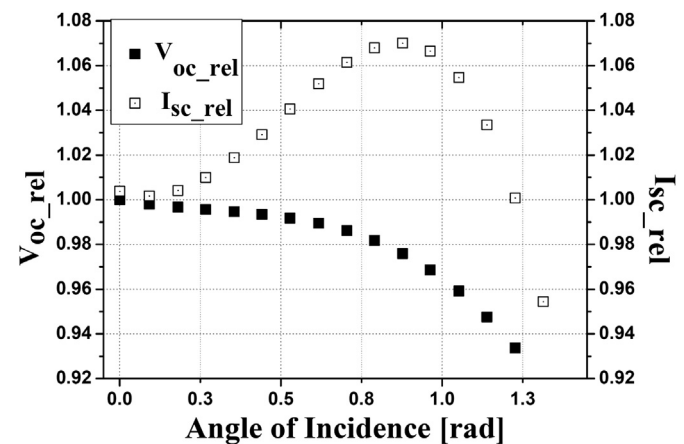
Fig. 4. Measured open circuit voltage/short circuit current relationship with the angle of incidence (in radians) for a DSSC.
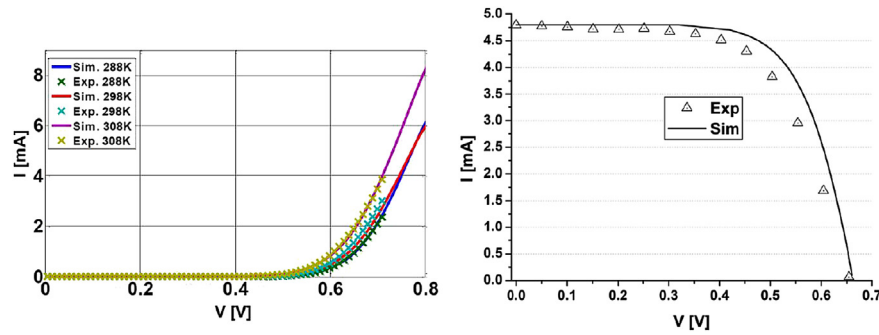
Fig. 5. Comparison of the simulated and experimentally measured I–V curves of the DSSC under (left) no light conditions, different operation temperatures and the (right) AM1.5 condition at a 300 K operating temperature.

data occurs and this is due in part for the manufacturing defects and also because the dark current model was used to build the solar cell mode of the DSSC. It is reminded that this procedure was used because the solar simulator equipment could not be placed in an incubator to control the DSSC temperature above and below room temperature. However, this model can still acceptable for dynamic system simulations [23]. Under such operating conditions, the energy conversion efficiency of the DSSC is about 7.3%, which is in similar accordance to the value of 7% from the manufacturer. Using DSSCs as the auxiliary power source is much better than silicon solar cells, especially under part light conditions and high incidence angles. This is the reason why this type of inexpensive, non-toxic and flexible solar cells should be employed for vehicle applications.

4.2. Non-ideal passivity based current controller performance

The buck converter modeled here is given in Table 3, where the switching frequency, inductor and capacitor value are taken from Ref. [21] to make a case comparison. The model is simulated in SimPowerSystems included in MATLAB/Simulink with a continuous simulation type, a variable step ode23t solver and a "robust" solver reset method for improved accuracy. A programmable pulse generator is devised to generate the digital gate signals, G and $\overline{G}$, for the power MOSFETs and merely needs a pulse period, which is the inverse of the switching frequency, and the pulse width, which is the ratio of the average duty cycle calculated with eqn. (9). The results of the dynamic passivity based controllers are shown in Fig. 6 for an R_i value of 0.85. The performance is quantified by the RRE (relative runtime error) expressed in percentages and equals to the ratio of the error and the expected value; in this case I_{dem}. It is clear to see that the idealized controller may have a large average RRE of 7.3% at steady state when operating at 18.5 A and missing I_{dem} by 1.5 A. If two or more TECs were to work at their full capacity, then the errors would be much greater. On the other hand, the loss included mathematical model has an average RRE of 0.01% at steady state without increasing in higher currents because all of the losses are included.

A needed parameter is the buck converter efficiency, η_{buck}, which can be predicted with respect to the output current and given in the following relationship:

Table 3
Buck converter parameters.

Switching frequency [MHz]	1.6
r_{MOS1}, r_{MOS2}, r_{d2} [ohms]	0.1, 0.1, 0.01
r_L, r_C, [ohms]	0.001
L [µH]	10
C [µF]	40

$$\eta_{buck} = 0.987 - 0.00187 I_{buck} \tag{13}$$

where I_{buck} A is the output current that each of the buck converters must supply. If more TECs are connected in parallel for a single buck converter, more current must be drawn from the power bus and therefore, the electrical losses of the buck converter and external wiring will lower the overall system efficiency. Therefore, two things can be done to improve the system, connect less TECs in parallel which will increase the number of buck converters or increase the number of parallel TECs, reducing the strain on each individual TEC but will increase the overall system cost. This efficiency relationship will be exported to the macro-scale air conditioning system.

4.3. Air conditioner simulation results

In order to predict the performance of the macro-scale TEC air conditioner coupled with green energy power sources under different operating conditions (diagram shown in Fig. 7), three cases are proposed and given in Table 4. In this solid state air conditioner design, a set of flexible, thin-film DSSCs attached to the top side of the vehicle body are used as the auxiliary power supply for an electric vehicle. The data of the car model, lithium-ion battery pack and DSSCs are shown in Table 5. This particular TEC may operate at a 15.4 V, 20 A and at a temperature gradient of 68 K when a 177.8 W of cooling power is needed and is manufactured by TANDE with model number TEC1-127.20. The TEC air conditioner uses the perturb and observe controlled DSSC power first; if not enough, the stored power from the auxiliary high power lithium ion batteries is used, and at a last resource, the fuel cell; this last power source was not included in this study. It is assumed that when the TEC air conditioner is off, the DSSC module will provide all its converted power to the ancillaries inside the vehicle, e.g., vehicle state monitoring.

In all the cases, individual incidence angles between the sun and window/DSSC are calculated by employing a modified MATLAB embedded program written by Paul Voss of the Smith College. It can calculate the angle of incidence between the sun and a specific surface provided the latitude, Julian day, hour of the day, window/surface zenith angle and the window/surface azimuth angle. The angle of incidence can be calculated for each individual surface composed of a windshield, two lateral windows and the DSSC module and then used to calculated the irradiated energy on that surface. In all cases, the cabin temperature is left to obtain a steady state, upon which time the TEC air conditioner is turned on. At this time, the relative heat resistance between the TEC air conditioner and the cabin/outside environment is 0.17 W K^{-1}; the fans are operated at its maximum operating power of 2.64 W per fan. In addition, the beam and diffuse sun irradiance are set as 1000 and
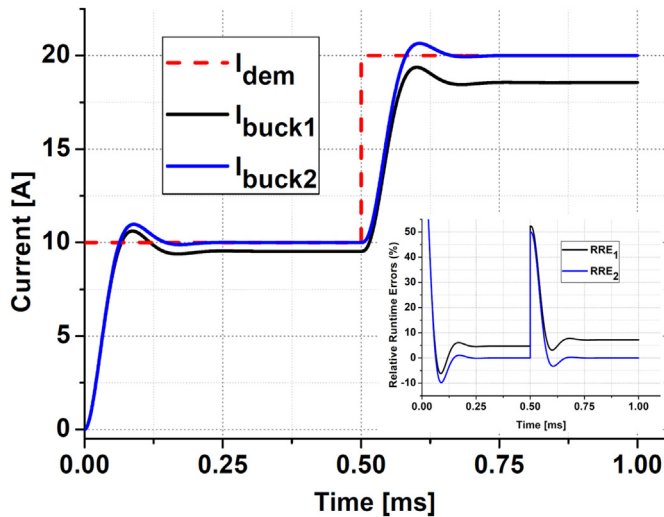
Fig. 6. Passivity-based current controller performance of idealized (I_{buck1}) and a loss-included (I_{buck2}) model. Inset: Relative run-time error of the models.

100 W m^{-2}; the diffuse irradiance is an extra power that silicon solar cells cannot fully use. The total demand current to be input to the passivity based current controlled buck converter array is in the form of a 0.1 proportional and 0.005 integral gain controller which measures and amplifies the error between the target and actual cabin temperature.

Fig. 8 (left, upper) and (left, lower) shows the prediction results for case 1. It can be seen that the TEC air conditioner, in order to counteract the heat effects of the windows and passengers, must operate in a steady state COP of 1.8–1.75. The COP calculation contains an initial spike because the current of each TEC is very low and thus, the COP is significantly higher in this short time. Following the steady state, the temperature difference between the target cabin temperature and the actual cabin temperature reaches 15 K; the target temperature is almost reached in 3 min. It is very important to notice that the DSSC module power is not enough and the LiB pack must supply around 225 W of extra power.

Case 2 is designed to study the performance of the TEC air conditioner under very hot ambient temperatures. From Fig. 8 (middle, upper), it can be seen that the COP of the TEC air conditioner does not have an exceptional performance and reaches a value above 0.5 at steady state. At this time, the LiB pack must

Table 4
Operating conditions of three case studies of the TEC air conditioner; windshield facing South, Julian date is 180, the Hsinchu City latitude is 24.8°N. Temperatures are in K.

Case 1: 9AM	Passenger number	2
	Ambient temperature	301
	Target cabin temperature	295.80
Case 2: 12AM	Passenger number	2
	Ambient temperature	308
	Target cabin temperature	295.80
Case 3: 12AM	Passenger number	2
	Ambient temperature	283.15
	Target cabin temperature	298.15

Table 5
Smart Fortwo data and balance of plant.

Windshield area [m^2], window zenith angle [deg]	0.915, 35.4
Lateral window area [m^2], window zenith angle [deg], amount	0.421, 72.7, 2
Lateral door area [m^2], window zenith angle [deg], amount	0.670, 90, 2
DSSC module area (car top) area [m^2]	1.270
Battery pack connection, max voltage [V], capacity [Ah]	14s2p, 3.65, 12
x_{TCC}, fan number	12, 4
Buck converter number (TECs per buck)	6 (2)

provide around 1100 W; almost entirely the demanded TEC module demand. Fig. 8 (middle, lower) shows that the target temperature is nevertheless met after approximately 7 min. The performance of the TEC air conditioner is not satisfactory for one reason; the rate of heat emission and absorbance at the sinks is not high enough and thus, the temperature difference between the emitting and absorbing side of the TEC module is too high − at which time, the heat transported through the thermal conductivity "bridge" is becoming predominant which in turn, reduces the COP. In order to solve this, it is suggested to increase the air velocity capability of the fans, create a diffuser type design to further increase the air velocity and turbulence in the sink or increase the number of TECs in order to minimize the strain. The model proposed here can easily enable engineers and researchers to study optimization designs as a first stage before solving computationally demanding 3D computational fluid dynamics coupled with thermal phenomena.

Finally, the third case is studied and the results are presented in Fig. 8 (right, upper) and (right, lower). In these conditions, the TEC air conditioner excels and achieves a COP of 1.72 even under a high temperature difference between the environment and the target temperature. This high COP enables the DSSC module to supply
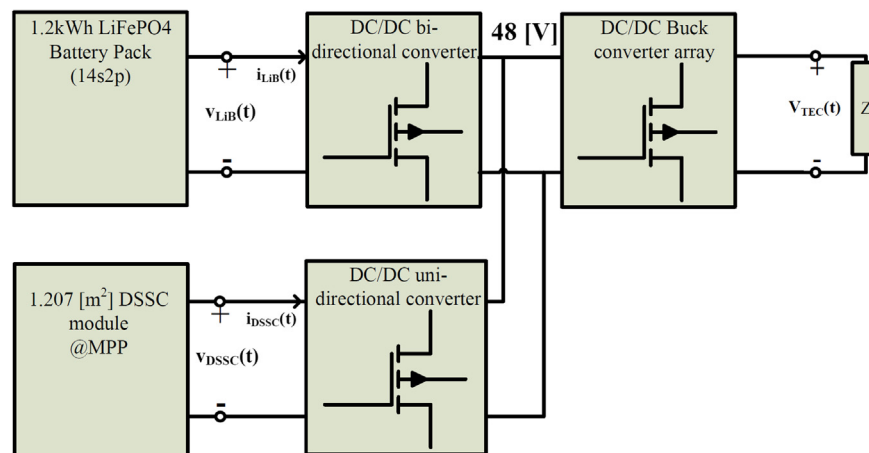
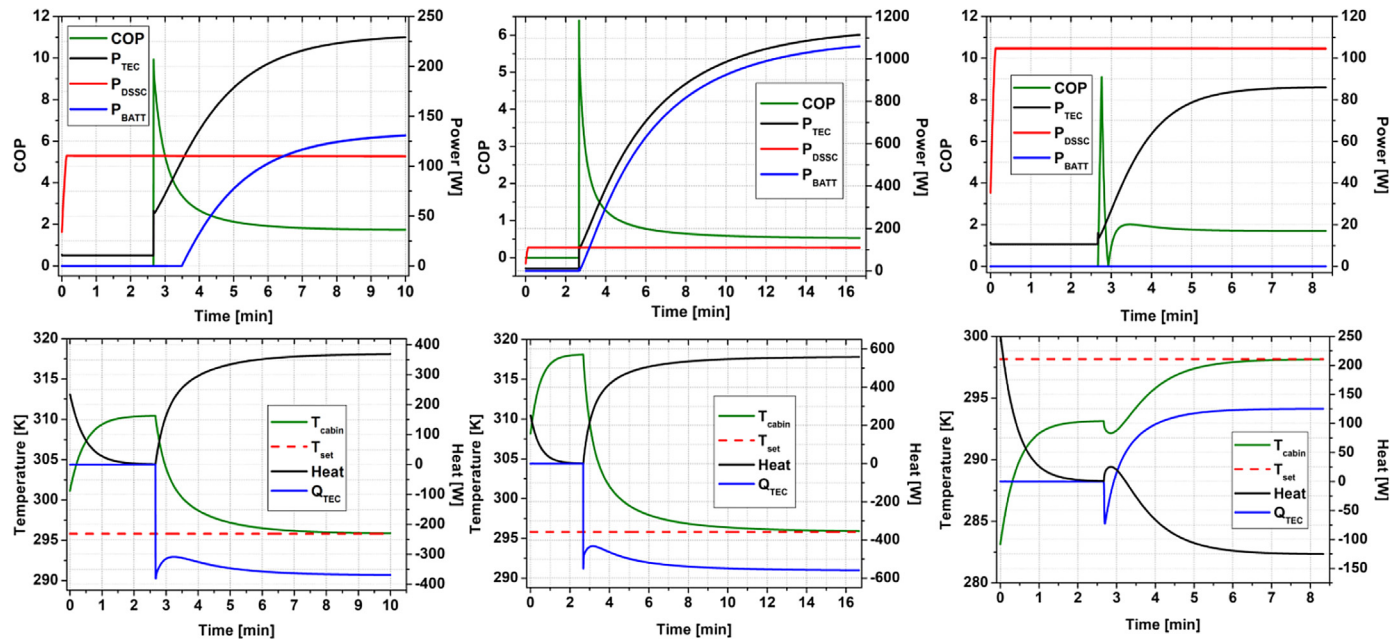**Fig. 7.** DSSC and LiB based TEC solid state air conditioner/heater power schematic.

Fig. 8. (upper) COP and electric power prediction results and (lower) cabin temperature, environmental cabin heat and TEC air conditioner performance prediction results for (left) case 1, (middle) case 2 and (right) case 3. Refer to Table 4 for details on each case.

almost all of the required power to the solid state air heater. The target cabin temperature may be reached in approximately 3 min. Under an even more careful inspection of Fig. 8 (right, lower), it can be observed that in the first 30 s of turning on the TEC module, the cabin temperatures experiences a small undershoot. This can be easily explained again with the thermal conductivity bridge inside the TEC modules; within the first seconds of a low electrical power supplied, the thermal conductivity effects, aided by the significant steady state temperature difference between the absorbing and emitting side, becomes predominant and, therefore, the cabin begins to lose heat through the solid state air heater. Therefore, it can be advised to have a lower limit of current, or voltage, to supply to the TEC modules which could provide a stronger heat pumping mechanism, preventing temperature undershoots and increasing the passenger comfort.

From these results, the most important requirement is to increase the turbulence which can be easily achieved by a higher air flow or by the use of an augmented sink connection, promising an increase in the heat convection coefficient by at least 10% when compared to traditional bonded heat fins. To further increase the system COP, present figures of merit of semiconductor materials have to be promoted 3–4 folds; this is under development using modern nanowire technologies [24]. Other alternatives can be to employ heat pipes or piezoelectric fans.

5. Conclusions

In this work, a new DSSC model, obtained by employing the diode mode and solar cell mode AC impedance extraction, is presented and proves to be accurate enough for dynamic system simulations. This green energy power source is interfaced to 48 V power net bus, combining efforts with a LiB pack. The solid state TEC air conditioner is connected to this power net bus with an array of buck converters designed with a loss included passivity controller for an extremely low steady state error. The inner passivity based controller, with included losses, eliminates the steady state error which can be extremely large at higher output currents if the idealized model is used. It was seen that the TEC air conditioning cooling system can be

switched to a heating pump with simple current reversal at the p and n junctions of the TEC module. These solid state air conditioners have the attractive advantage of being extremely lightweight with no need of refrigerants and, if designed well, may very well achieve a high COP and save space in small vehicles - also due to the reduced balance of plant. The current TEC cooling system is excellent in transient performance attaining a COP higher than 1.7 under mild environmental conditions and 0.55 under stringent ones, limiting applications in the later conditions at the current state of technology. Under air heating operating conditions, however, the TEC module excels and is predicted to achieve a COP higher than 1.7 in a relatively high demand condition. It is finally acknowledged that the success of TECs for electric vehicles may lie in the small size of the cabin air volume and improved isolation from outside heat. More importantly, the use of DSSCs offers more efficiency under part sunshine conditions and can absorb more beam and diffuse solar irradiance, which is not possible to achieve with silicon based solar cells.

Acknowledgments

References

[1] Daly S. Automotive air-conditioning and climate control systems. 1st ed. Amsterdam; Boston: Elsevier Butterworh-Heinemann; 2006.
[2] Riffat SB, Ma X, Wilson R. Performance simulation and experimental testing of a novel thermoelectric heat pump system. Applied Thermal Engineering 2006;26(5–6):494–501.
[3] Cosnier M, Fraisse G, Luo L. An experimental and numerical study of a thermoelectric air-cooling and air-heating system. International Journal of Refrigeration 2008;31(6):1051–62.
[4] Maneewan S, Tipsaenprom W, Lertsatitthanakorn C. Thermal comfort study of a compact thermoelectric air conditioner. Journal of Electronic Materials 2010;39(9):1659–64.

[5] Xiao JS, Yang TQ, Li P, Zhai PC, Zhang QJ. Thermal design and management for performance optimization of solar thermoelectric generator. Applied Energy 2012;93:33–8.

[6] Korzhuev MA, Katin IV. On the placement of thermoelectric generators in automobiles. Journal of Electronic Materials 2010;39(9):1390–4.

[7] Yella A, Lee H-W, Tsao HN, Yi C, Chandiran AK, Nazeeruddin MK, et al. Porphyrin-sensitized solar cells with Cobalt (II/III)–based redox electrolyte exceed 12 percent efficiency. Science 2011;334(6056):629–34.

[8] Xiaoting W, Waite N, Murcia P, Emery K, Steiner M, Kiamilev F, et al. Improved outdoor measurements for very high efficiency solar cell sub-modules. In: 2009 34th IEEE photovoltaic specialists conference (PVSC) 2009. p. 409–14.

[9] Chen WH, Miranda AG, Hong CW. Parametric studies on the photovoltaic performance improvement of a nanotube photo-electrochemical solar cell. Journal of The Electrochemical Society 2011;158(5):P57–64.

[10] Toyoda T, Sano T, Nakajima J, Doi S, Fukumoto S, Ito A, et al. Outdoor performance of large scale DSC modules. Journal of Photochemistry and Photobiology A 2004;164(1–3):203–7.

[11] Le Pierrès N, Cosnier M, Luo L, Fraisse G. Coupling of thermoelectric modules with a photovoltaic panel for air pre-heating and pre-cooling application; an annual simulation. International Journal of Energy Research 2008;32(14):1316–28.

[12] Barchowsky A, Parvin JP, Reed GF, Korytowski MJ, Grainger BM. A comparative study of MPPT methods for distributed photovoltaic generation. In: 2012 IEEE PES innovative smart grid technologies (ISGT) 2012. p. 1–7.

[13] Tofighi A, Kalantar M. Power management of PV/battery hybrid power source via passivity-based control. Renewable Energy 2011;36(9):2440–50.

[14] Miranda ÁG, Hong CW. Integrated modeling for the cyclic behavior of high power Li-ion batteries under extended operating conditions. Applied Energy 2013;111(0):681–9.

[15] Radziemska E. The effect of temperature on the power drop in crystalline silicon solar cells. Renewable Energy 2003;28(1):1–12.

[16] Cheng T-C, Cheng C-H, Huang Z-Z, Liao G-C. Development of an energy-saving module via combination of solar cells and thermoelectric coolers for green building applications. Energy 2011;36(1):133–40.

[17] Zhang ZM. Nano/microscale heat transfer. New York, NY: McGraw-Hill; 2007.

[18] Lineykin S, Ben-Yaakov S. Modeling and analysis of thermoelectric modules. IEEE Transactions on Industry Applications 2007;43(2):505–12.

[19] Levinson R, Pan H, Ban-Weiss G, Rosado P, Paolini R, Akbari H. Potential benefits of solar reflective car shells: cooler cabins, fuel savings and emission reductions. Applied Energy 2011;88(12):4343–57.

[20] Scherpen JMA, Jeltsema D, Klaassens JB. Lagrangian modeling of switching electrical networks. Systems & Control Letters 2003;48(5):365–74.

[21] Guo XH, Feng QY. Passivity-based controller design for PWM DC/DC buck current regulator. In: Lect Notes Eng Comp 2008. p. 875–8.

[22] Katrine Flarup J. Performance comparison of a dye-sensitized and a silicon solar cell under idealized and outdoor conditions. Technical University of Denmark; 2008.

[23] Fabregat-Santiago F, Bisquert J, Palomares E, Otero L, Kuang D, Zakeeruddin SM, et al. Correlation between photovoltaic performance and impedance spectroscopy of dye-sensitized solar cells based on ionic liquids. The Journal of Physical Chemistry C 2007;111(17):6550–60.

[24] Majumdar A. Thermoelectricity in semiconductor nanostructures. Science 2004;303(5659):777–8.